SAND2019-10799C

# Translating the Micro-scale to the Macro-Scale: Signatures of Fracture Evolution

L. J. Pyrak-Nolte
*Purdue University, West Lafayette, Indiana*

L. Jiang
*Purdue University, West Lafayette, Indiana*

A. Modiriasari
*Purdue University, West Lafayette, Indiana*

H. Yoon
*Sandia National Laboratories, Albuquerque, New Mexico*

A. Bobet
*Purdue University, West Lafayette, Indiana*

ABSTRACT: In this paper, the role of micro-scale properties and behavior on the detection of crack initiation, propagation and geochemical alteration is examined through three topics: (1) identification of a geophysical precursor for a system transitioning from meta-stability to unstable behavior with specific focus on crack nucleation, propagation and coalescence; (2) demonstration of acoustic emissions from geochemically-induced fractures; and (3) understanding the role of depositional layers and mineral fabric on tensile crack formation. The results from these studies advance current understanding of which microscopic properties of evolving fracture systems are most useful for predicting macroscopic behavior and the best imaging modalities to use to identify the seismic signatures of time evolving fracture properties.

## 1 INTRODUCTION

The recent growth in shale gas extraction, geothermal energy development and storage of anthropogenic gases and fluids has led to increased human interaction with the Earth's subsurface. A management challenge for these subsurface sites is to optimize extraction/storage approaches to yield maximum potential while minimizing risks. Fractures are one of the dominant factors that influence the success or failure of these management tasks because all subsurface activities perturb fluid pressures and stresses in rock, causing mechanical discontinuities to open, close, initiate, coalesce and/or propagate, while natural and engineered fluids can result in geochemical alterations that lead to crack growth. With the goal of sustaining production/isolation throughout the life-cycle of a subsurface site, it is necessary to detect and image fracture systems to monitor alterations as well as to link geophysical measurements to mechanical and hydraulic integrity of the subsurface rock.

Failure in rock is a progression of energy transfers from the smallest scales (lattice or microstructure) to potentially the full scale of a system under consideration. At the smallest scale, the mineral composition, distribution, orientation and bonding among minerals are known to affect the engineering properties of a rock in addition to the presence of structural features such as micro-cracks, layers and other sources of porosity. For example, Brace (1965) demonstrated exper-imentally that the anisotropy in the intrinsic elastic property of linear compressibility is effected by mineral crystal orientation based on measurements on rock with oriented mica, calcite and quartz at pressures of 0.2 to 0.9 GPa to remove the effects of micro-cracks. Agliardi et al. (2014) found that failure modes and uniaxial compressive stress depended on the orientation of loading relative to foliation in gneissic rock but with significant scattered in the values of UCS. While Chandler et al. (2016) demonstrated for shale the effect of the orientation of fine scale layering relative to loading direction on fracture toughness. They found that layer orientation alone was not suffi-cient to explain the observed anisotropy in fracture toughness.

One difficulty in performing experiments to link macro-scale behavior to micro-scale features and the composition of rock is the inherent presence of heterogeneity in mineral composition and structural features that can occur among samples taken from the same formation or block of rock, and even within a single sample. To overcome this difficulty, synthetic or analog rock has been used in the past to study the effect of specific structural features on rock behavior. Gypsum has been used as a model soft rock (Nelson, 1968) to study crack initiation, propagation and coalescence with designed flaws to generate specific crack types (Bobet & Einstein, 1998; Wong & Einstein, 2006; Park & Bobet, 2009), slip along mechanical discontinuities (Mutlu and Bobet, 2006; Hedayat et al., 2014a&b); and the effects of surface roughness on normal and shear stiffness of a fracture (Choi et al.2014). In many studies on the effect of fractures or mechanical discontinuities on compressional, P, and shear, S, wave propagation, planar or machined fractures in aluminum and other synthetic materials have been used to investigate the transition from displacement discontinuity behavior to resonant scattering (Nolte et al., 2000); cross-coupling stiffness (Nakagwa et al., 2000), and wave propagation in a medium with two orthogonal fracture sets (Shao & Pyrak-Nolte, 2016).

With the advent of 3D printing, also known additive manufacturing (Burns, 1993), the ability to control structural features and compositional homogeneity has improved such that samples can be "geo-architected". The concept of a geo-architected rock is a synthetic analog that is fabricated and structured in the laboratory using natural or synthetic constituents to develop controlled features and/or geochemistry/mineralogy in specimens that promote repeatable experimental behavior rock (Pyrak-Nolte & DePaolo, 2015; Mitchell & Pyrak-Nolte, 2018). Much work has been performed on controlling the structure in analog rock such as 3D printing in plastics or with polymers to reconstruct porosity or fracture surface roughness from X-ray tomographic scans and laser surface profiling (e.g. Ishutov et al., 2015; Jiang et al., 2016; Head & Vanorio, 2016; Suzuki et al., 2017). Polymer/resin-based and gypsum-based printers have been used to study dynamic crack coalescence (e.g. Jiang et al., 2016; Gell et al., 2018); mechanical behavior of fractured rock (Zhu et al., 2018); and elastic properties of material with penny-shaped inclusions (Huang et al., 2016). Some studies have combined 3D printing and analog materials to generate molds of fracture surfaces from which casts of fracture surfaces are made with cement (Woodman et al., 2017) or transparent acrylic to aid visualization (Boomsma et al., 2015). Casting processes enable control of the matrix properties in terms of strength, porosity and brittleness/ductility. While other research has focused on using powder forms of the constituent minerals in shale to form synthetic layered shale by subjecting the structured powder mixture to high pressures and temperatures (e.g. Luan et al., 2016; Gong et al., 2018).

In this paper, the role of micro-scale properties and behavior on the detection of crack initiation, propagation and geochemical alteration is examined through three topics where specific structural and/or compositional features are controlled to: (1) identify of a geophysical precursor for a system transitioning from meta-stability to unstable behavior with specific focus on crack nucleation, propagation and coalescence; (2) demonstrate the existence of acoustic emissions from geochemically-induced fractures; and (3) understand the role of depositional layers and mineral fabric on tensile crack formation. The results from these studies advance current understanding of which microscopic properties of evolving fracture systems are most useful for predicting macroscopic behavior and the best imaging modalities to use to identify the seismic signatures of time evolving fracture properties.

## 2 SIGNATURES OF ORIENTED MICRO-CRACKS DURING CRACK FORMATION

### 2.1 *Background*

The formation and growth of discontinuities in rock with natural and engineered processes cause instabilities such as infrastructures failure, rock slope instability, or slip along faults and earthquakes. Monitoring the time and location of crack formation and coalescence, and determination of the crack type (tensile or shear) are the challenges in the rock mass evaluation. Seismic wave imaging has been used in previous studies as a precursory method to crack formation and failures (Pyrak-Nolte & Roy, 2000; Modiriasari et al., 2017) and to slip along fractures (Chen et al., 1993; Nakagawa et al., 2000; Nagata et al., 2008; Hedayat et al., 2014; Rouet-Leduc et al., 2017). Modiriasari et al. (2017) have identified precursors associated with the initiation and propagation of tensile cracks with significant changes in the amplitude of the compressional (P) and shear (S)

waves. However, the shear crack initiation could not be detected from the P- or S-wave amplitudes. Nakagawa et al. (2000) showed that during shearing along a synthetic fracture, which can be idealized with an array of oriented microcracks, an incident S- or P-wave is converted to P- or S-wave, respectively, even for normal incident waves. Here, we show that converted waves emerge at the onset of damage in the form of shear cracks and provide precursory signatures to shear crack formation. The precursory signatures arise from the formation of oriented microcracks prior to coalescence.

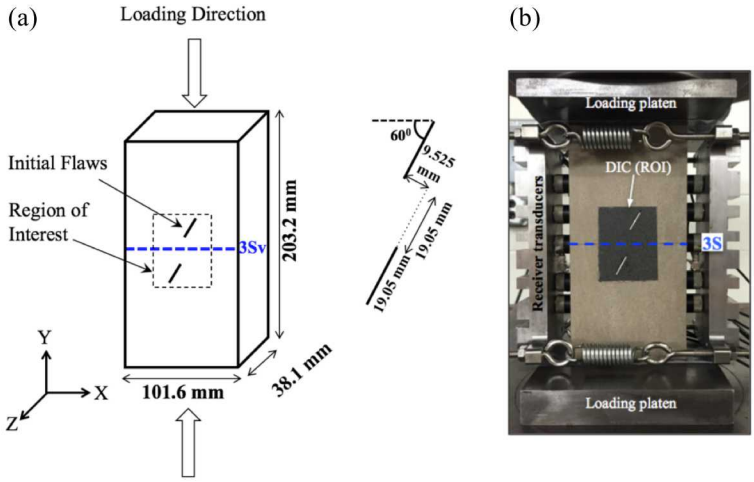


Figure 1. Sample and flaws geometry (a), and the experimental set-up for digital image correlation (DIC) on the Region of Interest (ROI) and seismic wave imaging (b).

## 2.2 *Experimental Set-up*

In the laboratory experiments, uniaxial compression loading was applied on several prismatic Indiana limestone specimens to investigate seismic precursors to the formation of shear cracks. The specimens contained designed flaws with specific geometries to induced shear cracks. The dimensions of the specimens were 203.2 × 101.6 × 38.1 mm (Figure 1a). The intact specimens had an average density of 2,326 kg/m$^3$, unconfined compressive strength of 47 MPa, Young's modulus of 7.4 GPa, and porosity of 15-25%. The average P- and S-wave velocities measured in the samples were 4,380 and 2,570 m/s, respectively. Two parallel designed flaws (cracks) were cut into the thickness of the specimen (Z direction in Figure 1a) using a scroll saw. Different geometries of the flaws were tested in the experiments (Modiriasari, 2017). The flaw geometry that is discussed in this paper is shown in Figure 1a. This geometry was selected because it is associated with the formation of shear cracks between the two flaws.

The formation of cracks on the surface of the specimen was detected using two-dimensional Digital Image Correlation (DIC) (Chu et al., 1985; Pan et al., 2009; Sutton et al., 2009) to measure surface displacements. DIC images were taken from the Region of Interest (ROI), gray region on the specimen surface in Figure 1b. A Grasshopper (Point Gray) CCD camera (with 2,248×2,048 pixels) and a Fujinon lense (Model HF50SA-1, with a focal length of 50 mm) were used to take images in the experiments. The details of the DIC analysis are explained in Hedayat et al. (2014), Modiriasari et al. (2017), and Modiriasari et al. (2018). An array of source and receiver transducers were placed on the sample's right and left side, respectively, to generate and propagate P- and S-waves into the specimen. The transducers were held in place using two steel plates and four springs with a tension of 70 kPa (Figure 1b). The lateral load was small enough to ensure that no lateral loading was applied on the specimen. The transducers had a central frequency of 1 MHz. Two pairs of transducers were used at the external tips of the flaws to monitor the formation of

tensile cracks. In addition, two pairs of transducers were used in the intact material for reference signals. The signals from transducer 3S will be analyzed in the next section because they probed between the two flaws, where the shear crack formed and the crack coalescence occurred. The 3S transducer pair was polarized vertically, in the Y direction.

The transducers were coupled on the specimen surface using a thin layer of oven-baked honey (at 90℃ for 90 minutes). The specimen surface was covered by plastic tape to prevent the penetration of honey into the sample pores. Initially, the sample was loaded in the uniaxial direction (using Instron loading machine and two steel loading plates as shown in Figure 1b) at a stress of 2 MPa for four hours to stabilize the seismic signals in a constant amplitude. Then the uniaxial load increased at a rate of 0.04 mm/min until the specimen failed. A thin Teflon film and petroleum jelly was used between the loading plates and the specimen surfaces to reduce the friction between the plates and the rock and the concentration of stresses on a sample. During loading, the applied load and displacements in the Y direction, two DIC images, and one full array of transmitted and reflected signals were recorded concurrently at a sampling rate of 1 Hz.

## 2.3 *Experimental Results*

### 2.3.1 *Digital Image Correlation (DIC)*

The path of crack formation interpreted from DIC results at different loads is shown in Figure 2. In the analysis, the crack initiation is identified when there was a minimum discontinuity of 5 $\mu$m in the horizontal displacement of two adjacent points. This threshold is greater than the noise in the measured displacements from the DIC and is large enough to determine the location of crack tips. The colorbar in the figure shows the aperture of the cracks (mm) inferred from the displacement discontinuity values. As shown in Figure 2b, the initiation of shear cracks was detected at the internal tips of the flaws at 88 kN. With uniaxial compression, the shear crack propagated until the coalescence occurred at 92 kN (Figure 2d). The aperture of the crack reached 60 $\mu$m at 105 kN (Figure 2f) and the specimen failed at 110 kN. Figure 2c shows that the signals from transducer 3S were roughly perpendicular to the path of shear crack formation.

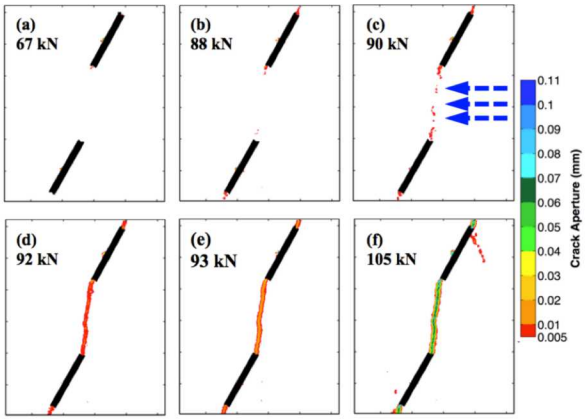


Figure 2. Initiation and propagation of cracks at the flaw tips, obtained from DIC, with load. The blue arrows denote that the incident wave between the two flaws were roughly perpendicular to the path of shear crack evolution.

### 2.3.2 *Seismic Wave Imaging*

#### 2.3.2.1 Transmitted Waves

Normalized amplitude of transmitted waves from traducer 3S with uniaxial load is shown in Figure 3. The amplitudes were extracted from wavelet analysis (Combes et al., 1989; Nolte et al., 2000; Polikar, 1999; Sheng, 1995) at a frequency of 440 kHz and were normalized with respect to the initial amplitude of the transmitted signal before increasing the load. The inset shows the waveforms of the transmitted signals arriving at ~42-44 $\mu$s at different loads. The normalized amplitude of the transmitted signals gradually decreased with load until ~90 kN. This is associated with the opening of microcracks inside the intact rock. The first significant change in the normalized wave amplitude occurred at ~92 kN, at the time of crack coalescence. This supports the previous finding that the shear crack initiation cannot be detected using the seismic wave transmissions (Modiriasari et al., 2017). However, the initiation of shear cracks was detected with the DIC at 88 kN. A minimum transmission of signals across the shear crack occurred after the crack coalescence and increase in the crack aperture

2.3.2.2 Converted Waves

Full waveforms of the signals were recorded during the experiment. The waveforms of the transmitted signals arriving between 22-40 $\mu$s at different loads are shown in Figure 4. S-wave transducers also generated small amplitude P-wave signals that had an arrival time of ~25 $\mu$s. At a load of ~67 kN, a new transmitted signal emerged in the waveforms and increased in amplitude with load up to 92 kN. The arrival time of this signal (34.7 $\mu$s) corresponded to the arrival time of a converted S- to P-wave, knowing the location of shear crack from the DIC results.

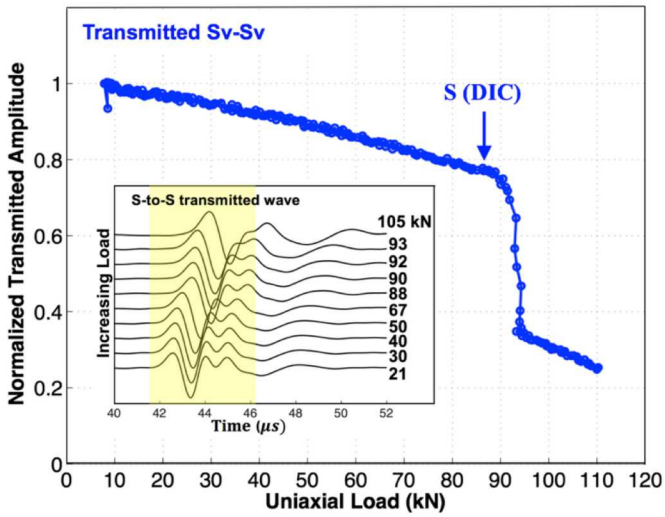


Figure 3. Waveforms and normalized amplitude of the transmitted signals from transducer 3S with uniaxial load. The blue arrow shows the load of the shear crack initiation detected using the DIC results.

The normalized amplitudes of the transmitted (blue) and reflected (green) waves (in the left axis), and converted (purple) waves (in the right axis) from transducer 3S, with uniaxial loads are shown in Figure 5. The reflected and converted wave amplitudes are normalized with respect to the initial value of the transmitted wave amplitude. The emergence of converted waves occurred at 67 kN, 76% of the crack detection load with DIC and 60% of the failure load. The converted wave amplitudes increased with shear crack propagation. With the crack coalescence, a significant drop in the transmitted wave amplitudes was observed. At this load, most of the energy of the wave was reflected from the surface of shear cracks and the reflected signals emerged and increased in amplitude.

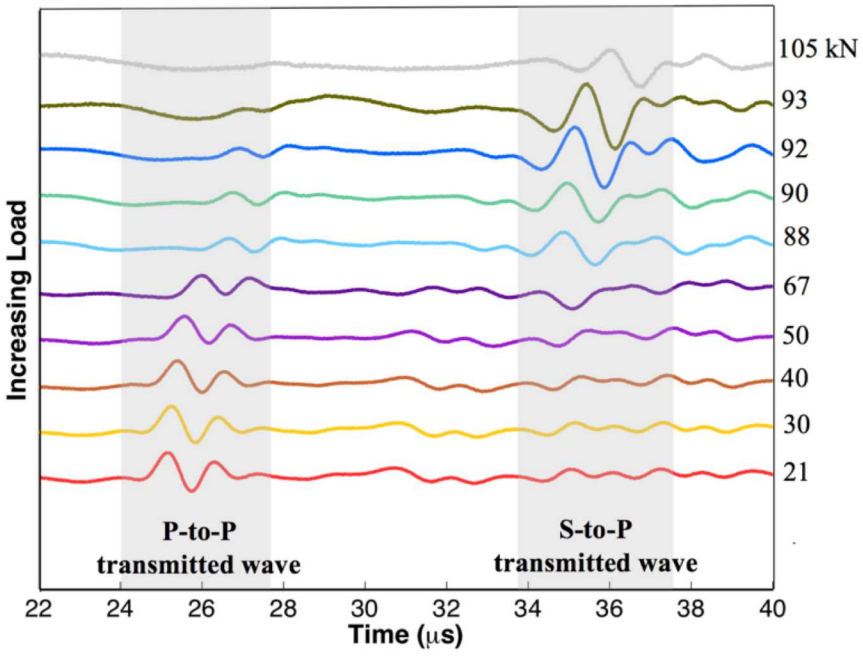


Figure 4. Waveforms of the transmitted signals arrived between 22 and 40 $\mu$s, as the load increased.

2.4 *Discussion*

The emergence of the converted waves is associated with the formation of an array of similarly oriented microcracks during shear crack growth. This is supported by the work of Nakagawa et al. (2000) that showed experimentally, theoretically, and numerically that information on the fracture void geometry is contained in P-S or S-P converted modes (P-compressional waves, S-shear waves). The conversions arise from a cross-coupling stiffness that can occur along rough surfaces. In their study, the microcracks in the array were oriented at 45° and -45°, and the cross-coupling stiffness was controlled through the application of shear and normal stress. They explained the experimental observations by extending the displacement discontinuity theory (Pyrak-Nolte et al., 1990; Schoenberg, 1980, 1983), and defining the cross-coupling fracture specific compliance (i.e. when a shear crack dilates, normal and shear stresses on a crack plane induce tangential and normal displacements, respectively). As a fracture is subjected to shearing, an array of similarly oriented microcracks forms that causes the cross-coupling compliance greater than zero and the emergence of converted S-P or P-S waves even at normal incidence. This affects the partitioning of energy to the transmitted, converted, and reflected wave phases. The converted phase is a function of the local-induced microcrack orientation prior to coalescence, the stiffness of the evolving damage zone, and the signal frequency. Jiang & Pyrak-Nolte (2018) used 3D printed arrays of micro-cracks with orientations (relative to the horizontal axis) from -90° to 90° to examine energy partitioning among the transmitted, reflected and converted modes using ultrasonic P and S wave transducers (Figure 6). In their study, the maximum amplitude in the converted mode occur for micro-crack orientations of +/- 45°. As shown by Nakagawa et al (2000) and observed in Figure 6, rotating the micro-crack 180° results in a signal with the same amplitude but 180° out of phase.

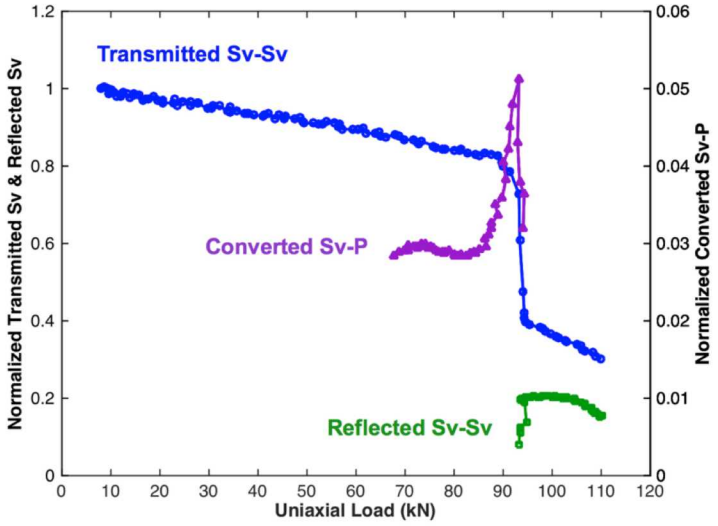


Figure 5. Normalized amplitude of the transmitted (blue), reflected (green), and converted (purple) waves from transducer 3S, as a function of load.

Here we observed the emergence of the S-P converted mode during shear crack formation but prior to coalescence for nearly normal incident waves. DIC showed that when the S-P converted mode emerges, micro-crack widths were on the order of 10 micrometers, a small fraction of the shear wavelength of 2.3 mm at 1 MHz. This suggest that a distributed array of oriented microcracks may form prior to coalescence and the extent of the array is sufficient to partition energy from the transmitted wavefront into a converted-mode but is not sufficiently open to partition energy into a reflected mode. Modiriasari et al. (2018) showed that relative amplitudes among the transmitted, reflected and converted modes observed in the data presented here is consistent with theoretical predictions for wave incident on a fracture at 10° and a cross-coupling factor of 0.75. The converted mode was also observed in the experiments when waves are obliquely

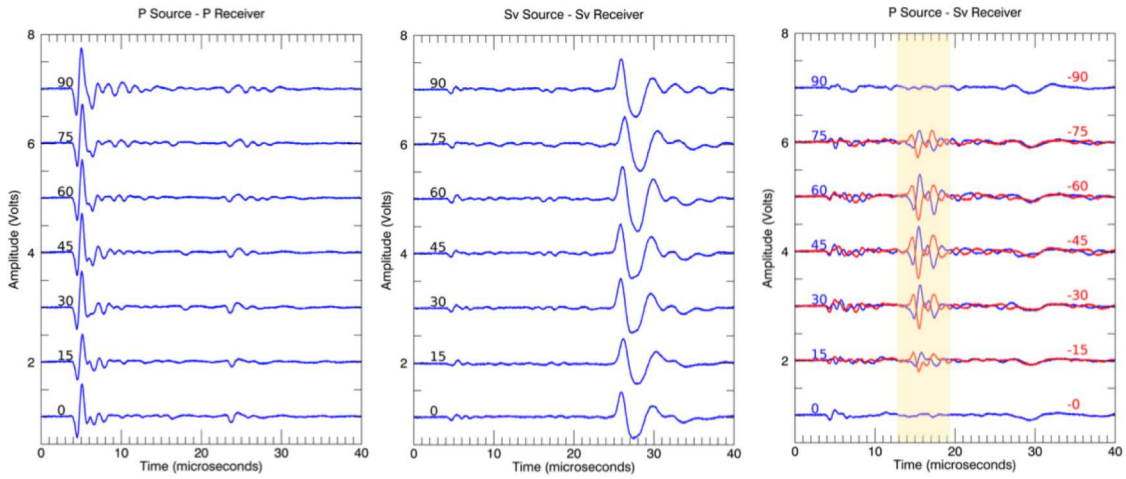


Figure 6. Example of received (left) compressional wave, (center) shear wave, and (right) S-P converted mode on 3D printed samples with oriented micro-cracks. The numbers represent the orientation of the micro-cracks relative to the horizontal. (right) Signals are shown from the sample positive (blue) and negative (red) orientations.

incident on a fracture (details are discussed in Modiriasari (2017)). The orientation of the inclined microcracks and stiffness of shear cracks were estimated using the theory and the relative changes in the wave amplitudes. This works illuminates how microstructural evolution during the crack formation affects macroscopic geophysical measurements.

## 3 GEOCHEMICAL-GEOMECHANICAL INTERACTIONS

### 3.1 *Background*

Volume expansion and contraction occur as minerals hydrate and dehydrate in response to changes in temperature, chemical absorption/desorption or other physical processes. This is of key importance for subsurface sites that contain shale with clay embedded in the matrix. Depending on the clay structure, certain clay minerals and clay bearing rock are capable of swelling as a function of the relative humidity, salt concentration or temperature (Tambach, et. al., 2004; Sone and Zoback, 2014). The charged layered structures and large reactive surfaces of clays introduce a complex relationship because of their reactivity with fluids, and play an important role in the mechanical behavior of the rock. Of the different types of clays, illite and montmorillonite-smectite are the most water-sensitive. Here, we use geo-architected rock to investigate geochemical-geomechanical coupling during dehydration.

### 3.2 *Geo-architected Synthetic Rocks*

#### 3.2.1 *Sample Preparation*

Geo-architected rocks were fabricated to determine the influence of clays and their respective geochemically-geomechanically driven volumetric alterations on geophysical properties, fracturing, and damage evolution in the microstructure of clay-rich structures during drying. The baseline for all samples is Ordinary Portland Cement (OPC Type I-II) and Ottawa Sand (SCS 250). All synthetic rocks are cured in a hot-water bath heated to +25$^{o}$ C. Samples were designed with localized clay volumes and with clay distributed throughout the matrix to examine the effect of clay distribution on fracture formation. For these two types of 20% clay-rich samples, the same proportions (by weight) of material used to create the baseline sample (referred to as the cement mortar sample) was used with the addition of clay. The Montmorillonite clay was hydrated before adding it to the baseline mixture (Mitchell and Pyrak-Nolte, 2018). The clay-rich mixture was

casted using a cylindrical mold with an average diameter of ~38 mm and an average length ~76 mm. Samples were de-molded after 24 hours and subjected to curing at 25$^{o}$ C for a number of days.

### 3.3 *Experimental Methods*

Samples were monitored during drying to determine if the dehydration of clay induced any physical changes in the geo-architected samples. The methods of characterization are described below.

#### 3.3.1 *Sample Characterization*

X-ray micro-tomography was performed to determine if any changes in the structure of the samples occurred during dehydration. A Zeiss Xradia 510 Versa - 3D X-Ray Microscope (3D XRM) was used to monitor the curing and drying of 1" diameter clay-rich samples over a 7-day period. The Versa system maintains an in-situ temperature of ~28$^{o}$C. Object Research Systems (ORS) Dragonfly Pro software was used to visualize and quantify the porosity and fracture network generated in the samples. FIJI (ImageJ) open source image processing package was also used for image analysis. The voxel edge length from the imaging was 40 micrometers.

#### 3.3.2 *Acoustic Emission Monitoring*

Clays are known to shrink or swell upon interaction with fluids (Wagner, 2013). Clay swelling or shrinkage can occur in the presence of pore-fluids and/changes in moisture content. Shrinkage can also occur upon drying. The extent of swelling depends on the amount and type of clay minerals, their fabric and the stress conditions, as well as the permeability (Prinz and Strauß, 2006; Wagner, 2013). Local volumetric changes caused by clay minerals in rock can cause crack initiation and growth, which in turn generates acoustic emissions. In addition to the behavior of clays in a matrix, drainage of fluids from porous media has been known to produce acoustic emissions (Michlmayr, 2012).

Acoustic-emission measurements were monitored to detect time-dependent crack formation in a sample during drying. The samples were monitored over a 7-day period using an array of six (6) broadband transducers (with flat frequency response between 20-400kHz (Physical Acoustics Corporation – F15-$\alpha$). The sensors were connected via preamplifiers to a Mistra/Physical Acoustics AE measurement system with a 5MHz sampling frequency. The threshold amplitude was set at 25dB. During monitoring, an AE signal was recorded when the signal amplitude exceeded an ascribed threshold.

### 3.4 *Results*

From the acoustic emission (AE) measurements, acoustic events were recorded on the cement-mortar sample and two samples with clay. In Figure 7a, acoustic emission events are shown for all of the samples. From X-ray tomographic samples (Figure 7d), no fractures or cracks were observed in the cement mortar samples. Unconnected porosity and the lack of any fractures for the cement mortar samples are observed in the 3D reconstruction shown Figure 8c and the AE events are attributed to movement of the air-water interface during drying. Moebius et al. (2012) demonstrated on glass bead packs that the movement of fluid-fluid interfaces resulted in measurable acoustic emissions. They attributed the AE events to Haines jumps, reconfiguration of fluids behind a drainage front, and also grain re-arrangement. They observed larger amplitude AE during drainage than during imbibition.

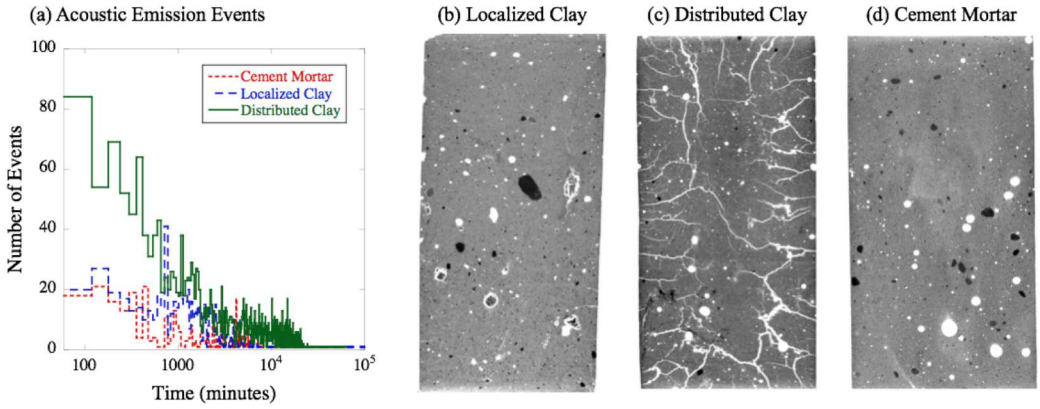


Figure 7. (a) Number of acoustic emission events as a function of time for the cement mortar, localized clay and distributed clay samples. 2D images from reconstructions of the X-ray tomograms for (b) localized clay, (c) distributed clay and (d) cement mortar samples. Air represents air.

When a sample contained clay that was localized as discrete balls, cracks were observed within the clay balls and around the clay balls as shown in the 2D cross-sections from the X-ray tomography data (Figure 7b). As the clay dehydrated, the shrinkage of the clay resulted in debonding from the cement-mortar matrix and cracking within the clay. However, from the 3D reconstruction of the X-ray tomograms (Figure 8 red regions), fractures connecting the clay balls are observed. The increase in acoustic emission around 600 minutes (Figure 7a) for the localized clay

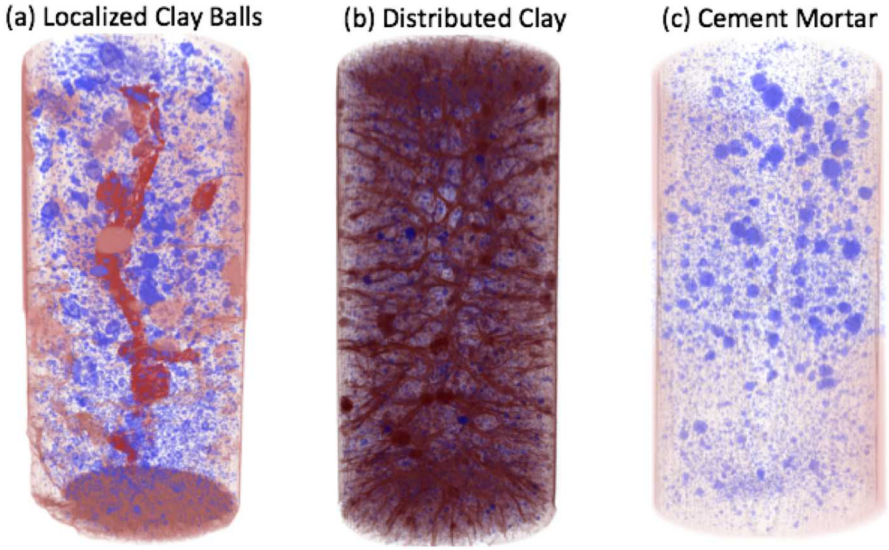


Figure 8. 3D reconstruction for X-ray tomograms from 25 mm diameter samples showing porosity (blue) and fractures induced from the shrinkage of clay (red) for (a) localized clay and (b) distributed clay. (c) The cement mortar samples contained no induced fractures, only unconnected porosity.

sample relative to the cement mortar sample is attributed to the initiation and propagation of the fractures that link the clay balls as water is released from the clay structure during dehydration.

Images of a geo-architected sample with distributed clay are shown in Figures 7c and 8b. The fracture network generated during the drying of the clay-rich geo-architected sample is extremely extensive extending from the exterior all the way through to the interior of the sample. This is consistent with the observed number events for the distributed clay sample which in the first 300 minutes had a factor of 2 to 4 times as many events as observed in the localized clay or the cement sample during that same period. These fractures were generated as a result of the chemo-mechanical behavior of clays, inducing fractures as the clay compacts and shrinks in volume.

### 3.5 *Discussion*

Examining the microstructure of geo-architected rocks after a period of drying with micro-CT has shown that the presence of clay can induce damage in a rock which would thereby affect the geophysical properties such as elastic moduli. The crack network formation is sufficient to generate measurable acoustic emission events. Previous work by Mitchell & Pyrak-Nolte (2018) has shown that these events have frequencies in 60 kHz – 250 kHz. Though these frequencies are much higher than traditional borehole sensors (20kHz), fiber optic-based distributed acoustic sensors with sensitivities on the order of nano-strains may have the potential to detect acoustic signatures from cracking induced by volumetric changes in minerals. The potential for geochemical-geomechanical coupling is high given the amount and different types of fluids that are pumped into the ground during fracturing activities. Future work will examine the effect of matrix strength on cracking and clay type using geo-architected samples.

## 4 TENSILE FRACUTRING: THE ROLE OF MINERAL TEXTURE AND LAYERING

A recognized challenge in quantifying the strength of rock is effect of layering which is well known to result in anisotropic rock properties and behavior. Anisotropy in rock arises from natural geological processes such as sedimentary processes where sediments are sequentially deposited in layers, and also from metamorphic processes that align minerals. For example, the complex response of shale is, in part, caused by anisotropy from layering within the rock and also from the mineral and organic components that compose the layers. The orientation of layers/bedding relative to in-situ and induced stresses can significantly affect rock strength and deformation because layers or interfaces between layers often behave as natural planes of weakness that can debond when stresses attain a failure condition.

From previous studies, rock strength has been shown experimentally to depend on the direction of fracture propagation relative to layering (Gao et al., 2017, Chandler et al., 2016, Na et al., 2017). In describing the relative orientations, the nomenclature often used is divider, short traverse and arrester (Figure 9). From experiments, fracture toughness is sometimes greatest for divider samples (e.g. Gao et al., 2017), while others have observed that the short traverse samples can exhibit both the largest and smallest values of fracture toughness (Chandler et al., 2016, Na et al., 2017). Variation in behavior relative to layering is often attributed to heterogeneity within a layer or among samples, the presence of clays, fluids, or organic material. A challenge in determining the effect of layer orientation on fracture toughness is rock variability. Here, geo-architected laboratory samples with repeatable mineral fabric and structural features were used to improve current understanding of the role of layering on peak failure load or fracture toughness in layered material. In this study, we found that predictions of fracture resistance based on layer

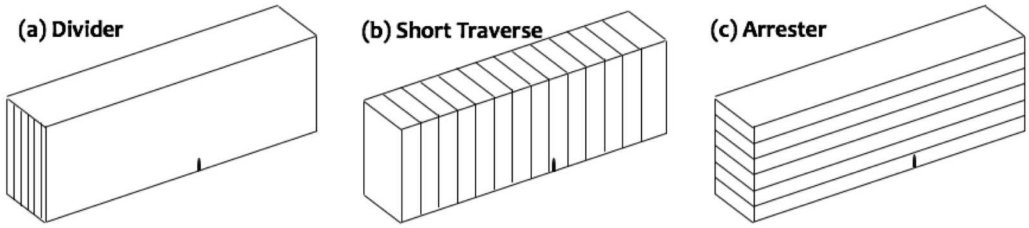


Figure 9. Sketch of nomenclature to describe layered samples.

orientation alone is insufficient. The presence of an oriented mineral texture within the layers also influences fracture toughness.

## 4.1 *Experimental Set-Up*

### 4.1.1 *Sample Preparation*

A 3D printing process (ProJet CJP 360 printer) was used to create layered geo-architected rock. A proprietary water-based binder (ProJet X60 VisiJet PXL) bonded layers of calcium sulfate hemi-hydrate (0.1 *mm* thick bassanite powders), resulting in a gypsum (calcium sulfate hemi-hydrate) reaction product. The direction of gypsum mineral growth is strongly affected by the direction of the binder application. The gypsum crystals form a bond between bassanite layers as one layer of bassanite is deposited on the previous layer. An oriented mineral texture forms because stronger bonds are formed amongst gypsum crystals than between gypsum crystals and bassanite powder.

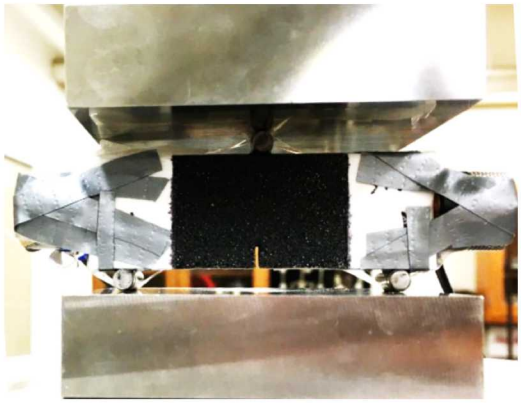

Fig. 10. Experimental setup: 3PB sample with top and bottom rods, acoustic transducers attached, and a speckled region on front surface for DIC.

With the aid of 3D printing, orientation between the bassanite layers and gypsum texture were controlled to examine the effect of texture direction relative to layer direction on mode I crack growth. Specimens were printed with dimensions of 25.4 x 76.2 x 12.7 *mm* with a 5.08 *mm* long 1.27 *mm* wide central notch. Tensile fractures were induced through three-point bending (3PB) experiments to induce a mode I crack from the central notch. In this paper, the 3D printed samples used in the study included: two short traverse samples with mineral textures perpendicular (sample V) and parallel (Valt) to the direction of fracture propagation, and two arrester samples with mineral textures parallel to layering but perpendicular to the fracture plane (H) and parallel to the fracture plane (Halt). For additional information on these samples, please see Jiang et al (2019).

For comparison, a cast gypsum sample was created to act as a standard. First, a resin-based 3D printer (FormLabs 2) produced a solid resin sample with the same dimensions as the 3D printed gypsum samples. The solid resin sample was used to fabricate a silicon rubber mold that was filled a mixture of gypsum and water and then vibrated to minimize the amount of trapped air. The cast gypsum samples were then cured in an oven at 40 °*C* for 4 days. The resulting cast gypsum sample had no preferred direction of mineral orientation.

### 4.1.2 *Tensile Fracturing*

Figure 10 shows a digital image of the three-point bending (3PB) method for inducing a tensile fracture (Mode I) in the 3D printed and cast samples. A rod is centered at the top of the sample and two additional rods are place along the bottom of the samples. Load was applied to a sample using an ELE International Soil Testing load frame with a 2000 *lbs* (8896 *N*) applied a load to a sample that was recorded with a capacity S-shaped load cell. A loading rate of 0.03 *mm/min* was applied to the sample while load and displacement were rec-orded at a 5 *Hz* MSamples/sec.

## 4.2 *Results*

### 4.2.1 *3 Point Bending Results*

Figure 11 provides the load-displacement data for four 3D printed geometries and for a cast gypsum sample. The strongest sample was the arrester sample H that had a mineral texture perpendicular to the direction of fracture propagation. As a tensile fracture to propagate in sample H, gypsum-to-gypsum bonds were broken. However, for the second arrester sample, Halt with mineral texture parallel to the induce fracture plane, the peak strength was 20% less than that observed for sample H. The two short traverse samples (V and Valt) exhibited similar peak loads that were the lower in magnitude than those for samples H and Halt. Cast gypsum samples that did not have a preferred mineral texture orientation were stiffer than the 3D printed samples and exhibited post-peak brittle behavior. The 3D printed sample, on the other hand, had relatively ductile post-peak behavior (Figure 11).

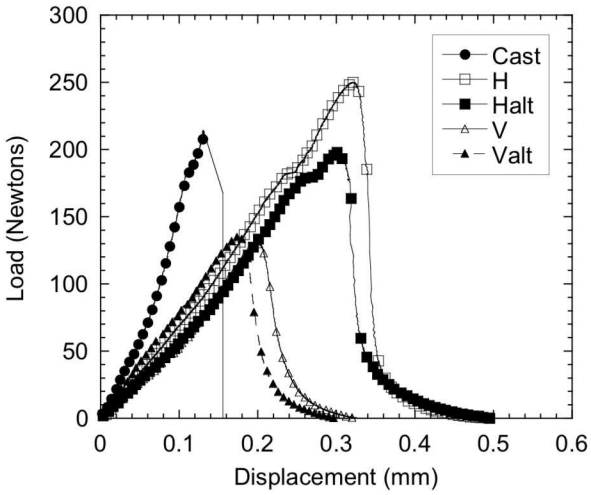


Fig. 11. Load vs. displacement for cast gypsum and 3D printed gypsum samples.

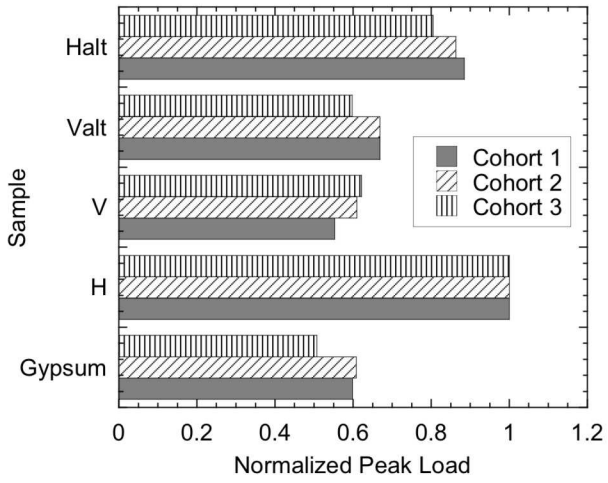


Figure 12. Normalized peak load by sample for 3 testing cohorts.

Three cohorts of cast gypsum and 3D printed samples H, Halt, V and Valt were tested (Figure 12). Peak load, which is linearly related to fracture toughness (Whittaker et al., 1992), is observed to depend on both the orientation of the bedding relative to the load and on the orientation of the mineral texture relative to the layering (Figure 11). The short traverse samples (V and Valt) exhibited consistently lower peak strengths than the arrester samples (H and Halt). Sample H exhibited the largest values of peak load and is used to normalize the peak load for all samples. In sample H both the mineral texture orientation and layering were perpendicular to the failure plane. Failure in the short traverse samples is dominated by debonding of the bassanite layers with mineral orientation slightly affecting the peak load. Peak loads at failure were on average found to be greater for the Valt than sample V which is attributed to the difference in the direction of mineral texture between the two samples. Halt samples, with mineral texture parallel to the induced tensile fracture plane, exhibited peak failure loads that were on average 15% lower than those for Halt.

### 4.3 *Discussion*

Geo-architected and analog gypsum samples enabled exploration of the effect of layer and mineral texture orientations on peak load achieved as a tensile fracture was induced. Additional testing has shown that the observed trends in peak failure load are consistent in terms the ranking of peak strength and the relative orientation between the layers and mineral texture. The greatest failure loads where obtained when the mineral texture direction was perpendicular to the fracture plane, and the smallest when the layering is parallel to the fracture plane. The 3D printed and cast gypsum samples exhibit some variability (Figure 12) but less variation than that observed in natural rock samples. Future directions will include testing on divider samples (Figure 9a) and examination of the effect of mineral texture on tensile fracture geometry.

## 5 CONCLUSIONS

The goal of experimental laboratory-based research is to design controlled experiments to illuminate fundamental physical behavior of materials subjected to controlled conditions. The field of laboratory rock physics is a fascinating field because rock is not a simple, uniform material, but is structurally and compositionally complex with features and heterogeneity occurring over a range of length scales. In this paper, we present several short examples of the use of crafted or geo-architected samples to explore and provide basic insight into contribution of microscale texture and structure on macro-scale measurements.

The study on the emergence of a precursor to failure during shear crack initiation and propagation was possible through the design of pre-existing flaws that generate shear cracks under uniaxial loading conditions. The precursor to failure is a compressional to shear wave converted mode that is associated with oriented micro-cracks. Though the micro-cracks are 1/100 of the scale of the wavelength of the probing signal, an array of oriented but disconnected micro-cracks is sufficient to generate a signature in the macro-scale measurements by elastic waves. This occurs because a surface of discontinuity in material properties, even if the discontinuity arises from small-scale heterogeneity much smaller than a wavelength, generates energy partitioning among macroscopic scattered fields.

The work on geo-architected rock with clay provides a method for examining the effect of volumetric shrinkage of minerals on the formation of fractures in a sample. The distribution of clay affects both the geometry of the fracture network that is formed and the acoustic emissions that are released during the fracture network formation. As part of an ongoing study, these geo-architected samples are enabling us to study how clay type (i.e. degree of swelling/shrinkage, chemical composition of the clay), clay distribution, fluid chemistry, and matrix strength effect the formation of fracture networks during dehydration processes. The goal is to provide insight into role of fluid chemistry during fluid injections/withdrawals into subsurface rock on the formation and accumulation of damage in samples with minerals that swell and shrink.

Finally, the 3D printed gypsum samples enabled experiments to determine why the strength of a layered sample differs from the expected behavior. Often, rocks are viewed as transversely isotropic because of layering in the sample. This study showed that in addition to layering, mineral texture orientation can have a significant role in the peak failure load. A determining factor is whether bonding between layers or bonding among oriented minerals within a layer is stronger. This suggests that mineralogy studies of specimens to determine if the minerals with layers are randomly oriented or align could provide insight into potential failure behavior of a rock specimen prior to testing.

3D printing has many advantages for studying specific structural and compositional distributions found in rock such as repeatable dimensions, composition and access to numerous samples. However, there are several drawbacks that include: the smallest feature size is often limited by the printer resolution, material behavior might not be purely brittle as some rock types,

and currently limitations in materials with which to print. However, advances in additive manufacturing are ongoing as the need for 3D printing continues in construction (Wu et al., 2016) and especially in the area of 3D printing habitable structures on the Moon from lunar soils (Cesaretti et al., 2014; Meurisse et al., 2018).

## 6 ACKNOWLEDGEMENTS:

The authors acknowledge support of the work related to geochemical-geomechanical coupling in geo-architected samples supported by the U.S. Department of Energy, Office of Science, Office of Basic Energy Sciences, Geosciences Research Program under Award Number (DE-FG02-09ER16022). We also acknowledge support from the EVPRP Major Multi-User Equipment Program 2017 at Purdue University for acquisition of the Zeiss Xradia 510 Versa 3D X-ray Microscope. From work related t o tensile fractures in 3D printed geo-architected work we acknowledge Sandia National Laboratories. Sandia National Laboratories is a multi-mission laboratory managed and operated by National Technology & Engineering Solutions of Sandia, LLC, a wholly owned subsidiary of Honeywell International, Inc., for the U.S. Department of Energy's National Nuclear Security Administration under contract DE-NA0003525. This work is supported by the Laboratory Directed Research and Development program at Sandia National Laboratories. This paper describes objective technical results and analysis. Any subjective views or opinions that might be expressed in the paper do not necessarily represent the views of the U.S. Department of Energy or the United States Government. The research presented in this paper related to the emergence of converted elastic wave modes during shear crack initiation and formation has been supported by the National Science Foundation, Geomechanics and Geotechnical Systems Program, with award number 1162082-CMMI. All of this support is gratefully appreciated.

## 7 REFERENCES

Agliardi, F., Zanchetta, S., and G. B. Crosta. 2014. Fabric controls on the brittle failure of folded gneiss and schist. *Tectonphysics*. v.637. 150-162.

Bobet, A. and Einstein, H.H. 1998. Fracture Coalescence, In Rock-Type Materials Under Uniaxial and Biaxial Compression. *International Journal of Rock Mechanics, Min. Sci. and Geomechanics Abstract*, Vol. 35, No. 7, pp. 863-889.

Boomsma, E. and L. J. Pyrak-Nolte. 2015. Chapter 5: Particle swarms in smooth-walled fractures. in *American Geophysical Union Monograph: Fluid Dynamics in Complex Fractured-Porous Systems*. Eds. B. Faybishenko, S. M. Benson and J. E. Gale. John Wiley & Sons, Inc. Hoboken, NJ. 65-84.

Brace, W.F. 1965, Relation of elastic properties of rocks to fabric. *Journal of Geophysical Research*. v. 70. no. 22. 5657-5667.

Burns, M. 1993. *Automated fabrication: improving productivity in manufacturing*. Prentice Hall. Englewood Cliffs. 369 p.

Cesarettie, G., Dini, E., De Kestelier, X., Colla, V. and L. Pambaguian. 2014,. *Acta Astronautic*. v 93. 430-450.

Chandler, M.R., Meredith, P.G., Brantut, N., Crawford, B.R. 2016. Fracture toughness anisotropy in shale. *Journal of Geophysical Research: Solid Earth*, 121 (3), pp. 1706-1729

Chen, Q.-Y., Lovell, C. W., Haley, G. M., & Pyrak-Nolte, L. J. 1993. Variation of shear-wave amplitude during frictional sliding. *International Journal of Rock Mechanics and Mining Sciences*. 30(7). 779–784. https://doi.org/10.1016/0148-9062(93)90022-6.

Choi, M.-K., Pyrak-Nolte, L.J. and A. Bobet. 2014., The effect of surface roughness and mixed-mode loading on the stiffness ratio Kx/Kz for fractures. *Geophysic.* 79:5. D319:D331.

Chu, T. C., Ranson, W. F., & Sutton, M. A. 1985. Applications of digital-image-correlation techniques to experimental mechanics. *Experimental Mechanics*. 25(3). 232–244. https://doi.org/10.1007/BF02325092

Combes, J., Grossmann, A., & Tchamitchian, P. 1989. Wavelets: Time-frequency methods and phase space. *The Journal of the Acoustical Society of America*. 89(5). 2477–2478. https://doi.org/10.1121/1.400986

Espinoza, D.N. and J.C. Santamarina. 2012. Clay interaction with liquid and supercritical CO2: The relevance of electrical and capillary forces. *International Journal of Greenhouse Gas Control*. 10: 351-362.

Galan, E. and R.E. Ferrell. 2013. Genesis of Clay Minerals. *Developments in Clay Science*. ch. 3: 83-126.

Gao, Y., Liu, Z., Zeng, Q., Wang, T., Zhuang, Z., Hwang, K.-C. 2017. Theoretical and numerical prediction of crack path in the material with anisotropic fracture toughness. *Engineering Fracture Mechanics*. 180. pp. 330-347.

Gell, E.M., Walley, S. M., and C.H. Braithwaite. 2018. Review of the validity of the use of artificial specimens for characterizing the mechanical properties of rock. *Rock Mechanics and Rock Engineering*. https://doi.org/10.1007/s00603-019-01787-8.

Gong, F., Di, B., Wei, J., Ding, P., Li, H. and Dingyuan Li. 2018. Experimental investigation of the effects of clay content and compaction stress on the elastic properties and anisotropy of dry and saturated synthetic shale. *Geophysics*. 10.1190/geo2017-0555.1, **83.** 5. (C195-C208).

Head, D., and T. Vanorio. 2016. Effects of changes in rock microstructures on permeability: 3-D printing investigation. *Geophys. Res. Lett*. 43. 7494–7502. doi:10.1002/2016GL069334.

Hedayat, A., Pyrak-Nolte, L. J., & Bobet, A. 2014. Detection and quantification of slip along non-uniform frictional discontinuities using digital image correlation. *Geotechnical Testing Journal*. 37(5).20130141. https://doi.org/10.1520/GTJ20130141 .

Hedayat, A., Pyrak-Nolte, L.J. and A. Bobet. 2014a. Multi-modal monitoring of slip along frictional discontinuities. *Rock Mechanics Rock Engineering*. DOI 10.1007/s00603-014-0588-7.

Hedayat, A., Pyrak-Nolte, L. and Bobet, A. 2014b. Detection and Quantification of Slip along Non-uniform Frictional Discontinuities using Digital Image Correlation. *ASTM Geotechnical Testing Journal*. DOI: 10.1520/GTJ2013.

Huang, L., Stewart, R.R., Dyaur, N. and J. Baez-Franceshi. 2016. 3D-printed rock models: Elastic properties and the effects of penny-shaped inclusions with fluid substitution. Geophysics. v. 81, no. 6. (NOVEMBER-DECEMBER 2016); P. D669–D677.

Huggett, J.M. and P.J.R. Uwins. 1994. Observations of waterclay reactions in water-sensitive sandstone and mudrocks using an environmental scanning electron microscope. *Journal of Petroleum Science and Engineering*. 10: 211-222.

Ishutov, S., Hasiuk, F. J., Harding, C. and J. N. Gray. 2015. 3D printing sandstone porosity models. *Interpretation*. August 2015. 3(3),SX49-SX61.

Jiang, C., Zhao, G-F., Zhu, J., Zhao, Y-X., and L. Shen. 2016. Investigation of dynamic crack coalescence using a gypsum-like 3D printing material. *Rock Mechanics and Rock Engineering*. v. 49. 3983-3998.

Jiang, L. and L.J. Pyrak-Nolte. 2018. Elastic wave conversions from fractures with oriented voids. *52nd US Rock Mechanics / Geomechanics Symposium*. Seattle, Washington. USA. 17–20 June 2018. ARMA 18-1204.

Jiang, L., Yoon, H., Bobet, A., and L.J. Pyrak-Nolte. 2018, Effect of Mineral Orientation on Roughness and Toughness of Mode I Fractures. *53rd US Rock Mechanics / Geomechanics Symposium*. New York, New York, USA. 17–20 June 2019. ARMA 19-0483.

Jiang, Q., Feng, X., Gong, Y., Song, L., Ran, S. and J. Cui. 2016. Reverse modelling of natural rock joints using 3D scanning and 3D printing. *Computers and Geotechnics*. v. 73. p210-220.

Luan, X., Di, B., Wei, J., Zhao, J. and X. Li. 2016. Creation of synthetic samples for physical modelling of natural shale. *Geophysical Propsecting*. v64. 898-914.

Meurisse, A., Makaya, A., Willsch, C. and M. Sperl. 2018, Solar 3D printing of lunar regolith. *Acta Astronautica*. v.152, 800-810.

Mitchell, C.A. and L. J. Pyrak-Nolte. 2017. Microstructural controls on the macroscopic behavior of geoarchitected rocks. *Proceedings of the 52th US Rock Mechanics / Geomechanics Symposium.* Seattle, WA, USA. June 17-20, 2017. ARMA 18-1235.

Mitchell, J.K. and K. Soga. 2005. *Fundamentals of Soil Behavior*. 3rd ed. Wiley.

Modiriasari, A. 2017 *Geophysical Signatures of Fracture Mechanisms*, Ph.D. Thesis. Purdue University. West Lafayette, IN. 135 pages.

Modiriasari, A., Bobet, A., & Pyrak-Nolte, L. J. 2017. Active seismic monitoring of crack initiation, propagation, and coalescence in rock. *Rock Mechanics and Rock Engineering*. 50(9). 2311–2325. https://doi.org/10.1007/s00603-017-1235-x .

Modiriasari, A., Pyrak-Nolte, L. J and A. Bobet. 2018. Emergent wave conversion as a precursor to shear crack initiation. *Geophysical Research Letters*. v 45. issue 18, 9516-9522.

Moebius, F., Canone, D. and D. Or. 2012. Characteristics of acoustic emissions induced by fluid front displacement in porous media. *Water Resources Research*. v.48, W11507, doi:10.1029/2012WR012525.

Mutlu, O. and Bobet, A. 2006. Slip Propagation along Frictional Discontinuities. *International Journal of Rock Mechanics and Mining Sciences*. Vol. 43. pp. 860-876.

Na, S., Sun, W., Ingraham, M. D., & Yoon, H. 2017. Effects of spatial heterogeneity and material anisotropy on the fracture pattern and macroscopic effective toughness of Mancos Shale in Brazilian tests. *Journal of Geophysical Research: Solid Earth*. 122(8). 6202-6230.

Nagata, K., Nakatani, M., & Yoshida, S. 2008. Monitoring frictional strength with acoustic wave transmission. *Geophysical Research Letters*. 35. L06310. https://doi.org/10.1029/2007GL033146.

Nakagawa, S., Nihei, K. T. T., & Myer, L. R. 2000. Shear-induced conversion of seismic waves across single fractures. *International Journal of Rock Mechanics and Mining Sciences*. 37(1-2). 203–218. https://doi.org/10.1016/S1365-1609(99)00101-X.

Nelson, R. 1968. *Modeling a jointed rock mass*. M.S. Thesis. Massachusetts Institute of Technology, Cambridge.

Nolte, D. D., Pyrak-Nolte, L. J., Beachy, J., & Ziegler, C. 2000. Transition from the displacement discontinuity limit to the resonant scattering regime for fracture interface waves. *International Journal of Rock Mechanics and Mining Sciences*. **37**. 219-230.

Pan, B., Qian, K., Xie, H., & Asundi, A. 2009. Two-dimensional digital image correlation for in-plane displacement and strain measurement: A review. *Measurement Science and Technology*. 20(6). 062001. https://doi.org/10.1088/0957-0233/20/6/062001.

Papaliangas, T.T. 1996. *Shear behavior of rock discontinuities and soil-rock interfaces*. PhD. Thesis. University of Leeds.

Park, C.H., and Bobet, A. 2009. Crack coalescence in specimens with open and closed flaws: a comparison. *International Journal of Rock Mechanics and Mining Sciences*, Vol. 46, pp. 819-829.

Polikar, R. 1999. The wavelet tutorial. I*nternet Resources: http://engineering.rowan.edu/polikar/WAVELETS/WTtutorial.html*.

Prinz, H., Strauß, R. 2006. Abriss der Ingenieurgeologie, fourth ed. Spektrum Akademischer Verlag , Oxford, 671 Sposito, G. 1989. *The Chemistry of Soils*, Oxford University Press , New York.

Pyrak-Nolte, L. J., Myer, L. R., & Cook, N. G. W. 1990. Transmission of seismic waves across single natural fractures. *Journal of Geophysical Research*. 95(B6). 8617. https://doi.org/10.1029/JB095iB06p08617.

Pyrak-Nolte, L. J., & Roy, S. 2000. Monitoring fracture evolution with compressional-mode interface waves. *Geophysical Research Letters*. 27(20). 3397–3400. https://doi.org/10.1029/1999GL011125.

Pyrak-Nolte, L.J., and D. J. DePaolo. 2015. *Controlling subsurface fractures and fluid flow: a basic research agenda*. Department of Energy Roundtable Report. DOI: 10.2172/1283189

Rouet-Leduc, B., Hulbert, C., Lubbers, N., Barros, K., Humphreys, C. J., & Johnson, P. A. 2017. Machine learning predicts laboratory earthquakes. *Geophysical Research Letters*. 44. 9276–9282. https://doi.org/10.1002/2017GL074677.

Schoenberg, M. 1980. Elastic wave behavior across linear slip interfaces. *The Journal of the Acoustical Society of America*. 68(5). 1516–1521. https://doi.org/10.1121/1.385077.

Scrivens, W. A., Luo, Y., Sutton, M. A., Collette, S. A., Myrick, M. L., Miney, P., & Li, X. 2007. Development of patterns for digital image correlation measurements at reduced length scales. *Experimental Mechanics*. 47(1). 63-77.

Shao, S. and L. J. Pyrak-Nolte. 2016. Elastic wave propagation in isotropic media with orthogonal fracture sets. *Rock Mechanics and Rock Engineering*, DOI 10.1007/s00603-016-1084-z

Sone H. and M.D. Zoback. 2014. Time-dependent deformation of shale gas reservoir rocks and its long term effect on the in situ state of stress. *International Journal of Rock Mechanics & Mining Sciences*. 69: 120-132.

Srodo′n, J., V.A. Drits, D.K. McCarty, J.C.C. Hsieh, and D.D. Eberl. 2001. Quantitative XRD analysis of clay-rich rocks from random preparations. *Clays, Clay Miner*. 49: 514–528.

Srodo′n, J. 2010. Evolution of mixed-layer clay minerals in prograde alteration systems. In: Fiore, S., Cuadros, J., Huertas, F.J. (Eds.), Interstratified Clay Minerals. Origin, Characteristics and Geochemical Significance. *AIPEA Educational Series*, vol. 1. Digilabs, Bari, Italy, pp. 114–175.

Suzuki, A., N. Watanabe, K. Li, and R. N. Horne. 2017. Fracture network created by 3-D printer and its validation using CT images. *Water Resour. Res*. 53. 6330–6339. doi:10.1002/2017WR021032.

Tambach, T., P.G. Bolhuis, and B. Smit. 2004. Angew. *Chem. Int.* ed. 2650 -2652.

Wagner, J.F. 2013. Mechanical Properties of Clays and Clay Minerals. Ch. 9: pp. 347-381. *Developments in Clay Science*. vol. 5A.

Woodman, J., Murphy, W., Thomas, M. E., Ougier-Simonin, A., H. Reeves and T. W. Berry. 2017. A novel approach to the laboratory testing of replica discontinuities: 3D printing representative morphologies. *American Rock Mechanics Association - ARMA 17-049.*

Whittaker, B.N., Singh, R.N., Sun, G., 1992. *Rock Fracture Mechanics—Principles, Design and Applications*. Elsevier, Amsterdam.

Wong, L., and Einstein H.H. 2006. Fracturing Behavior of Prismatic Specimens Containing Single Flaws. *Proceedings of the 41st U.S. Symposium on Rock Mechanics*. Golden, Colorado. Paper 06-899

Wu, P., Wang, J. and X. Wang. 2016. A critical review of the use of 3-D printing in the construction industry. *Automation in Construction*. v. 68, 21-31.

Zhu, J.B, Zhou, T., Liao, Z. Y., Sun, L., Li, X.B., and R. Chen. 2018. Replication of internal defects and investigation of mechanical and fracture behaviour of rock using 3D printing and 3D numerical methods in combination with X-ray computerized tomography. *International Journal of Rock Mechanics and Mining Sciences*. v. 106, 198-212.